metals

MDPI

Article

Damage Prediction in the Wire Drawing Process

Álvaro González [1], Marcela Cruchaga [2], Diego Celentano [3] and Jean-Philippe Ponthot [4,*]

[1] Escuela de Ingeniería Mecánica, Pontificia Universidad Católica de Valparaíso, Quilpué 2430000, Chile; alvaro.gonzalez.o@pucv.cl
[2] Departamento de Ingeniería Mecánica, Universidad de Santiago, Estación Central 9160000, Chile; marcela.cruchaga@usach.cl
[3] Departamento de Ingeniería Mecánica y Metalúrgica, Pontificia Universidad Católica de Chile, Macul 7810000, Chile; dcelentano@uc.cl
[4] Department of Aerospace and Mechanical Engineering, Université de Liège, 4000 Liège, Belgium
* Correspondence: jp.ponthot@uliege.be

Abstract: In this study, the prediction of damage in the wire drawing process of 2011 aluminum alloy was investigated through both experimental and numerical methods. A comprehensive experimental setup was designed involving 20 cases of wire drawing with varying die angles (10°, 15°, 21°, 27°, and 34°) and reductions (21%, 29%, 31%, and 38%). Each case was tested three times, and the drawing forces, as well as occurrences of wire breakage, were recorded. The mechanical behavior of the material was firstly characterized using uniaxial tensile tests, whose results were used to determine the material parameters of both the hardening Voce law and those of uncoupled and coupled damage models. Then, the numerical simulations of the wire drawing process were performed using a finite element model, accounting for axisymmetric conditions and mesh convergence analysis to ensure accuracy. The previously characterized damage models were applied to evaluate their fracture prediction capabilities. A novel presentation method using three-dimensional graphs was employed to indicate the level of damage for each angle and reduction, providing greater sensitivity and insight into the damage values. Good agreement between the experimental and numerical data was demonstrated for the bilinear coupled damage model, validating its effectiveness. This study contributes to a better understanding of damage prediction in the wire drawing process, with implications for improving industrial practices and material performance evaluations.

Keywords: aluminum alloy; wire drawing; damage prediction; drawing limit diagram

Citation: González, Á.; Cruchaga, M.; Celentano, D.; Ponthot, J.-P. Damage Prediction in the Wire Drawing Process. *Metals* **2024**, *14*, 1174. https://doi.org/10.3390/met14101174

Academic Editor: Gang Fang

Received: 31 August 2024
Revised: 8 October 2024
Accepted: 14 October 2024
Published: 16 October 2024

1. Introduction

The wire drawing process is recognized as a critical manufacturing technique for producing wires with precise dimensions and enhanced mechanical properties. Significant attention has been garnered in recent research due to the complexity of the process and the challenges associated with predicting material damage during deformation [1–4]. Historically, the prediction of damage in wire drawing has been addressed through various experimental and numerical methods [5,6]. The use of finite element analysis (FEA) has become standard practice for simulating the wire drawing process and assessing the behavior of the material under deformation [7,8].

An essential contribution to the understanding of damage prediction in metal-forming processes was made by Alberti et al. [9]. A finite element model combined with the Oyane fracture criterion [10] was developed to predict the occurrence of the central bursting defects in wire drawing. This study provided a theoretical framework that allowed for the identification of safe and unsafe zones in the process based on the reduction in area and the semicone die angle. This approach proved effective in aligning numerical predictions with experimental results, offering a robust method for evaluating material performance and preventing defects in industrial applications.

Building upon the foundational work of Alberti et al., Reddy et al. [11] further explored the ductile fracture criteria by comparing multiple approaches, including the hydrostatic stress criterion. The study validated the conservative nature of the hydrostatic stress criterion, which offered safer predictions compared to the Oyane criterion, aligning more closely with experimental results. This progression highlights the evolution in predictive accuracy for defect formation in metal-forming processes.

Significant contributions to the field of defect prediction in wire drawing were made by McAllen and Phelan [12] through the development of a numerical model that identifies safe and unsafe zones for drawing 2011 aluminum alloy wire. By utilizing a 2D map that relates die semi-angles to area reductions, their research delineated a 'nose-shaped' curve that separates process conditions that prevent the occurrence of internal defects, such as central bursts, from those that promote them. The validity of this approach was supported by comparisons with experimental data from the work of Orbegozo [13], providing a clear visual tool for optimizing drawing parameters and avoiding failures during production.

Haddi et al. [14] significantly advanced the understanding of defect formation in copper wire drawing by developing a numerical model that delineates safe and chevron crack-prone zones. The Cockcroft and Latham [15] fracture criterion was utilized to map the influence of die semi-angles and area reductions on the likelihood of central bursts. The resulting 2D map demonstrated that higher die angles and reductions increased the risk of chevron crack formation while lower semi-angles and reductions provided safer drawing conditions.

Cho et al. [16,17] conducted an extensive evaluation of various ductile fracture criteria to predict material failure in the cold drawing process of high-alloy steel. By integrating six different fracture models into finite element analysis, 2D maps were generated to delineate critical zones where fractures are likely to occur based on die semi-angle and reduction ratios. The findings demonstrated that criteria incorporating stress triaxiality and maximum principal stress, such as the Ko et al. [18] criterion, provided higher prediction accuracy, especially in challenging drawing conditions with higher reduction ratios and die angles. Expanding on their previous research, Cho et al. [19] introduced a Process Condition Diagram (PCD) that maps critical zones in the bar drawing process, particularly highlighting conditions that lead to microdefects and fractures. By applying multiple damage models and validating their predictions through finite element analysis, the study confirmed that the Ko criterion, which considers stress triaxiality and maximum principal stress, provided the most accurate predictions for high-alloy steel.

In accordance with the studies presented previously, traditional methods often utilize two-dimensional plots such as the drawing limit diagram (DLD), which maps angle versus reduction and marks fracture and non-fracture cases using appropriate symbols. While these methods are effective, they may not be detailed enough to capture subtle variations in damage levels across different drawing conditions. In this study, a comprehensive experimental and numerical approach is adopted to predict damage in the wire drawing process of 2011 aluminum alloy. A novel contribution of this work is the introduction of a three-dimensional wire drawing limit diagram (3D-DLD) that correlates die angles, reduction ratios, and accumulated damage. This 3D map provides a more direct and nuanced visual understanding of the damage levels developed under various geometric configurations and according to different damage criteria. By offering a more integrated view of how these parameters interact, this research advances our understanding of damage prediction in the wire drawing process and proposes potential improvements for industrial practices and material performance evaluations.

2. Material and Methods

2.1. Material

The raw material consists of 2011 aluminum wire rods with two different diameters (6.00 and 6.35 mm). These are considered as entry diameters ($D1$) in Figure 1. The 2011 aluminum alloy studied in this work is a high-strength material primarily used for ma-

chining purposes. As part of the 2000 series, it is characterized by the addition of copper as the principal alloying element, which significantly enhances its mechanical properties. This alloy offers excellent machinability and good mechanical strength. Its composition and characteristics make it suitable for applications requiring accurate and high-speed machining, such as in the manufacturing of complex parts and components. The chemical composition of the alloy was determined using optical emission spectroscopy, and the results are summarized in Table 1.

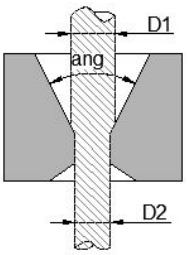

Figure 1. Schematic of the drawing die and wire rod.

Table 1. Chemical composition of 2011 aluminum alloy (wt%) obtained by optical emission spectroscopy.

Al %	Cu %	Si %	Fe %	Mn %	Mg %	Cr %	Zn %	Ti %	Bi %	Sn %	Pb %
92.12	5.97	0.36	0.52	0.008	0.004	0.004	0.004	0.008	0.49	0.004	0.49

2.2. Modeling

The mechanical response of the material can be described by local governing equations expressed by the mass conservation, linear momentum balance, and the dissipation inequality using an elastoplastic model with damage while considering the von Mises yield function.

2.2.1. Damage Evolution

Kashanov [20] introduced the concept of damage to define a variable that quantifies the degradation of the mechanical properties of a material. This variable is essential in damage mechanics as it allows the accumulation of microstructural defects, such as voids and microcracks, to be quantified. The damage variable (d) is correlated with reductions in stiffness, strength, and ductility, and its evolution ($\dot{d}$) can be described as:

$$\dot{d} = f_i \, \dot{\bar{e}}_p \tag{1}$$

where $\dot{\bar{e}}_p$ is the effective plastic strain rate and f_i is a damage function that varies depending on the model or approach used.

In the context of predicting fractures in various processes, classic damage models are employed to evaluate the integrity and failure of materials. These models are broadly categorized into uncoupled and coupled damage models, each providing a distinct approach to characterize material behavior under stress.

Uncoupled damage models: These damage models quantify a damage variable which does not affect the material constitutive behavior. Various uncoupled models have been proposed in the literature, for example, Freudenthal [21], Cockcroft and Latham [15], or Rice and Tracey [22]. The damage function of these classic models is described in Table 2, where $\bar{\sigma}$ corresponds to the von Mises equivalent stress, σ_1 to the maximum principal stress, and ξ, known as the triaxiality ratio, corresponds to the ratio between the mean stress and the von Mises equivalent stress.

Table 2. Uncoupled damage functions.

Damage Model	Damage Function f_i
Freudenthal	$\bar{\sigma}$
Cockcroft and Latham	σ_1
Rice and Tracey	$0.283 \exp\left(\frac{3}{2}\xi\right)$

Coupled damage models: In this approach, the calculated damage variable affects the material constitutive model. Building on the original work proposed by Lemaitre [23], Celentano and Chaboche [24] formulated the evolution equation for this internal variable as follows:

$$\dot{d} = A_d \frac{Y}{Y_{1D}} \dot{\bar{e}}_p \tag{2}$$

where A_d represents the slope of the $d - \bar{e}_p$ curve under uniaxial stress conditions and Y denotes the damage-strain energy release rate, with Y_{1D} acting as the value of this variable under uniaxial stress conditions. The damage-strain energy release rate Y is defined as:

$$Y = \frac{\bar{\sigma}^2}{2\, E_0\, (1-d)^2} R_\nu \tag{3}$$

where E_0 is the Young's modulus of the undamaged material and R_ν is the stress triaxiality factor, which is expressed as:

$$R_\nu = \frac{2}{3}(1+\nu) + 3(1-2\nu)(\xi)^2 \tag{4}$$

where ν is the Poisson's ratio.

Recently, an extension of this approach has been proposed by González et al. [25,26] that incorporates a bilinear evolution of damage according to the following formulation:

$$\dot{d} = \begin{cases} 0 & ;\text{if } \bar{e}_p < \bar{e}_0 \\ \dfrac{d_i}{\bar{e}_i - \bar{e}_0} \dot{\bar{e}}_p & ;\text{if } \bar{e}_0 < \bar{e}_p \leq \bar{e}_i \\ \dfrac{d_c - d_i}{\bar{e}_c - \bar{e}_i} \dot{\bar{e}}_p & ;\text{if } \bar{e}_i < \bar{e}_p \leq \bar{e}_c \\ \dfrac{(1-d_c)^{\beta_d}}{\bar{e}_c - \bar{e}_0} \dot{\bar{e}}_p & ;\text{if } \bar{e}_c < \bar{e}_p \end{cases} \tag{5}$$

where $\bar{e}_0$ is the effective plastic strain at the onset of damage (threshold effective plastic strain), $\bar{e}_i$ is an intermediate effective plastic strain within the range $[\bar{e}_0 : \bar{e}_c]$ used to describe the bilinear damage function, $\bar{e}_c$ is the critical effective plastic strain (i.e., the plastic strain at fracture), d_i is the damage corresponding to $\bar{e}_i$, d_c is the critical damage, and β_d is a numerical parameter that characterizes the acceleration of damage once the critical damage is reached, representing the final stage of damage evolution up to the physical rupturing of the specimen.

2.2.2. Hardening Response

The hardening is assumed to be described by the Voce model expressed as:

$$\sigma_y = \sigma_0 + Q\left[1 - \exp(-b\bar{e}_p)\right] \tag{6}$$

In Equation (6) , σ_0 corresponds to the yield strength and Q and b are parameters specific to the model. The same hardening model is applied in both damage approaches; however, for the coupled model, the equivalent stress is modified by the damage. In uncoupled damage models, the damage value can be considered a post-process variable since it can be calculated at the end of the simulation, as it does not affect the constitutive relation

of the material. In contrast, for coupled damage models, the constitutive tensor is affected as the damage evolves, so the effective stress must be multiplied by $(1 - d)$ to account for the material degradation due to the presence of damage.

2.3. Hardening and Damage Characterization via Tensile Tests

The mechanical behavior of the material was characterized through uniaxial tensile tests conducted on wire rods with an initial length of 220 mm using a Zwick–Roell universal testing machine (ZwickRoell, Ulm, Alemania) with a load capacity of 100 kN. The tests were performed at a speed of 5 mm/min, and the force was recorded using the load cell of the universal testing machine. The strain was measured over a gauge length of 50 mm using digital image correlation (NCORR software, v1.2). From the true stress–strain experimental curves obtained in the tensile test, the elastoplastic parameters of the material (previously defined in Equation (6)) are determined using a least squares fitting method [25].

Uncoupled damage:

For uncoupled damage, the methodology to characterize the model is as follows:

1. Based on the stress–strain results obtained from tensile tests, a hardening model is characterized to describe the elastoplastic behavior of the material. The characteristic material parameters are determined, such as the modulus of elasticity, yield strength, hardening parameters, and fracture strain.
2. Using the previously characterized parameters, a numerical simulation of the uniaxial tensile test is performed on the wire rods until the equivalent strain reaches the experimental fracture strain.
3. From the numerical simulation results of the uniaxial tensile test, the damage is evaluated according to Equation (7).

$$d = \int_0^{\bar{e}^p} f_i d\bar{e}^p \tag{7}$$

By evaluating this integral over a range of equivalent plastic strain from zero to the fracture strain, the value considered as critical damage is obtained (See Equation (8)).

$$d_c = \int_0^{\bar{e}_f^p} f_i d\bar{e}^p \tag{8}$$

Bilinear coupled damage:

Following the methodology proposed by Gonzalez et al. [25], the characterization of the bilinear model is obtained using the following approach:

1. Load–unload tensile tests are conducted on the wire rods. The first loading is carried out to a value beyond the yield point, and, from the second loading onwards, the deformation level is gradually increased. This increment is performed successively until material fracturing is achieved. This approach allows damage to accumulate at different levels of plasticity.
2. From the stress–strain curve obtained from the cyclic load–unload tests, the modulus of elasticity at each unloading is calculated using the least squares linear regression technique.
3. Subsequently, damage is calculated using Lemaitre's proposed relationship:

$$d = 1 - \frac{E}{E_0} \tag{9}$$

4. With the damage versus strain curve, the bilinear model is fitted using a least squares fitting method.
5. Once the damage curve is obtained, the numerical simulation of the tensile test is performed by activating the coupled damage model using the initially obtained hardening parameters. Since the damage is now coupled to the constitutive relation of the

material, differences arise between the numerical and experimental results. Therefore, an iterative process must be carried out to recalculate the hardening parameters until a good match between the numerical and experimental results is achieved.

Damage Index: Since each approach or damage model has distinct damage functions, a comparison is proposed using a dimensionless parameter known as the damage index (Equation (10)). This index is defined as the ratio between the damage reached (d) and the critical damage (d_c, which corresponds to the damage value at the moment of fracture) regardless of whether a coupled or uncoupled approach is used. Introducing this index allows for easier and more direct comparisons between different models and approaches. Consequently, when the damage index equals 1, the fracture condition is predicted by the model.

$$I = \frac{d}{d_c} \tag{10}$$

2.4. Wire Drawing Tests

In this study, a series of laboratory drawing tests was conducted to evaluate the damage prediction in aluminum alloy wires. Ten dies with 5 varying angles and two different exit diameters ($D2$ according to Figure 1) were used.

The combination of die angles, entry diameters, and exit diameters resulted in 20 unique cases. Each of these cases was tested three times to ensure reliability and reproducibility. The details of the experimental design are summarized in Table 3. Henceforth, the following nomenclature will be used: a21r38 corresponds to the case with a 21° angle and a 38% reduction, as an example.

Table 3. Geometric variables for drawing tests.

Reduction (%)	Angle (°)	$D1$ (mm)	$D2$ (mm)
21	10	6.00	5.35
	15	6.00	5.35
	21	6.00	5.35
	27	6.00	5.35
	34	6.00	5.35
29	10	6.00	5.00
	15	6.00	5.00
	21	6.00	5.00
	27	6.00	5.00
	34	6.00	5.00
31	10	6.35	5.35
	15	6.35	5.35
	21	6.35	5.35
	27	6.35	5.35
	34	6.35	5.35
38	10	6.35	5.00
	15	6.35	5.00
	21	6.35	5.00
	27	6.35	5.00
	34	6.35	5.00

The measured data included the drawing force and the occurrence of wire breakage for each case were recorded. This experimental setup allowed for the impact of different angles, reductions, and entry diameters on the damage prediction in aluminum alloy wires to be analyzed.

2.5. Wire Drawing Simulation

The schematic representation of the spatial discretization used for the numerical simulations of the wire drawing process is shown in Figure 2. This figure represents a generic case rather than a specific one, as there are 20 different geometric configurations. The intention is to illustrate the comparison between both states (before and after contact), but it is not an exact representation of the finer mesh used in the simulations. The initial conditions are displayed at the top of the figure to describe the imposed constraints, while the drawing condition in the steady state (where numerical results are obtained) is presented at the bottom of the figure.

Axisymmetric conditions were adopted, and a uniform displacement (linearly dependent on time) was imposed at the end of the wire rod to ensure the complete passage of the material through the die in accordance with the drawing speed used in the experimental tests. Four-node quadrilateral elements were utilized for the spatial discretization of the wire rods (considered as deformable elements, with elastoplastic parameters being characterized in the tensile test), and two-node linear elements (considered as rigid elements) were used for the die. The length of the wire rod was chosen to ensure that the simulation reached a steady-state condition, recognizing that wire drawing is typically a continuous process. A mesh convergence analysis was previously performed to determine the element size that ensures no variations in the numerical results with a finer mesh, specifically analyzing the drawing force, as it is the variable used to compare the numerical and experimental results. Considering that 20 geometrically different configurations are studied, a convergence analysis was conducted for each one and an average number of representative elements for all cases was ultimately adopted, amounting to 2801 elements, of which 2500 are used to model the wire, 250 are used to model the contact between the wire and the die, and 51 are used to model the die. The numerical simulations were conducted using an 'in-house' finite element code that incorporates all the plasticity, contact, friction, and damage equations used in this study.

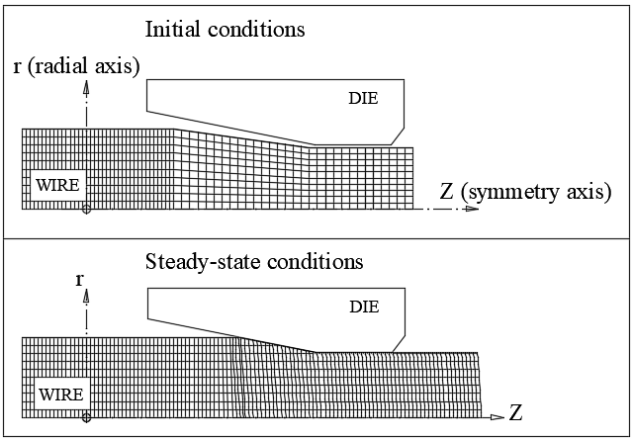

Figure 2. Numerical model for finite element simulation of the drawing process. The figure presents a schematic view of the numerical model. Adapted with permission from Ref. [25] 2022 International Journal of Damage Mechanics.

Each of the 20 cases presented in Table 3 was geometrically modeled, and an iterative process was conducted to obtain a single friction coefficient for all cases, ensuring that the drawing forces obtained numerically were similar to the experimental ones. The following methodology was used to determine the friction coefficient: First, 20 simulations (each representing the geometric cases presented in Table 3) were performed with an initial assumption of zero friction. The numerical results (specifically the drawing load) were then compared to the experimental data and the error associated with each case was calculated. Next, another set of 20 simulations was carried out with a friction coefficient of 0.01, and the numerical results were again compared to the experimental data, with the associated error

being calculated for this coefficient. This process was repeated until the average error was minimized. The best result was obtained when the friction coefficient was equal to 0.05. The methodology used in this study, where the friction coefficient is determined by comparing the numerical and experimental drawing forces, is a widely adopted approach in the literature [12]. While the ideal method would involve direct friction tests, in many cases, where such tests are not feasible, the adjustment of the friction coefficient based on experimental drawing forces offers a valid alternative. As mentioned above, this method has been applied in several studies involving wire drawing and metal-forming processes where the main goal was to match numerical predictions with experimental outcomes.

In summary, for the numerical modeling of the wire drawing process, the following steps are required:

- Provide material behavior information, which is previously obtained from the tensile test.
- Model and discretize the drawing cases to be studied using finite elements.
- Adjust the contact model to ensure proper correlation between experimental and numerical data.

With this, the damage models are subsequently implemented, which must be characterized according to the methodology detailed previously.

3. Results

3.1. Material Characterization

3.1.1. Hardening

The raw data from the tensile test are shown in Figure 3, including the force versus the elongation curve recorded by the universal testing machine during the wire rod tensile test. The engineering stress is calculated by dividing the force by the initial cross-sectional area, while the true stress is obtained by dividing the force by the instantaneous area. To determine the instantaneous area, the wire diameter is estimated at specific time intervals using digital image correlation (DIC) and the corresponding area is calculated. This diameter is also used to compute the logarithmic (true) strain. From the engineering and true stress–strain curves obtained from the tensile test, the elastic modulus is calculated using the least squares method in the linear elastic region. Additionally, the yield stress, which refers to the stress at which the material begins to deform plastically, is determined.

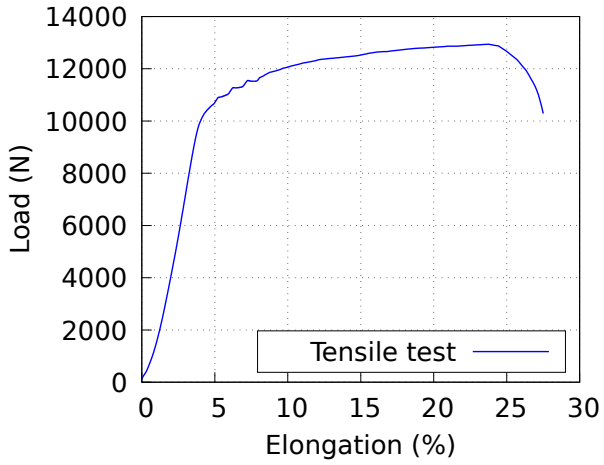

Figure 3. Raw tensile test data for wire rods, illustrating the load versus elongation behavior.

The results of the true stress–strain curve obtained from tensile tests performed on the 2011 wire are presented in Figure 4a, and fractured specimens are shown in Figure 4b. In the curve, the experimental results are observed, as are the numerical ones where hardening is fitted using the Voce model (Equation (6)). The mechanical parameters of the material are summarized in Table 4. It should be noted that the values of Q and b shown in parentheses correspond to those obtained when the coupled damage model is employed. As indicated

in Section 2.2, the stress–strain constitutive equation is influenced by damage, making it necessary to recalculate these values to accurately reflect the material behavior.

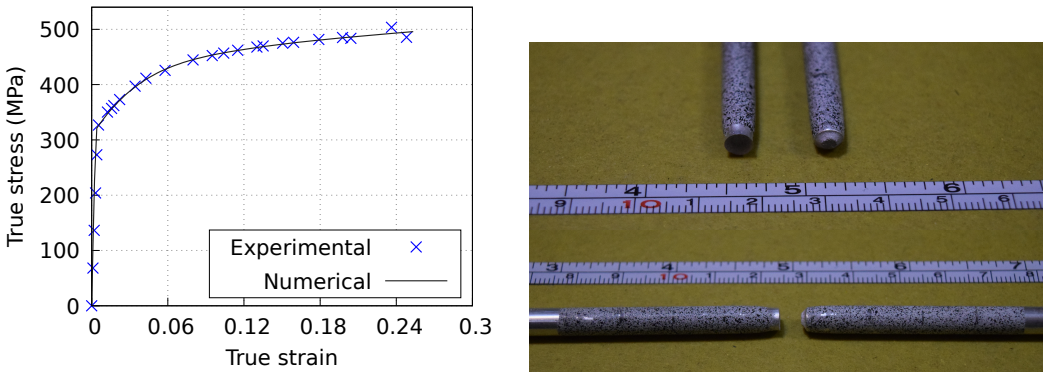

(**a**) (**b**)

Figure 4. Tensile test results for the wire: (**a**) stress–strain curve and (**b**) fractured specimen.

Table 4. Mechanical parameters of the material.

Parameter	Value
Modulus of Elasticity (GPa)	68.2
Yield Strength (MPa)	318
Fracture Strain (%)	24.8
Hardening Parameter Q (MPa)	155 (170.5)
Hardening Parameter b	23 (23.4)

3.1.2. Damage

In Table 5, the results obtained from characterizing each of the uncoupled damage models presented earlier in Table 2 are shown. As can be seen, the critical damage value differs for each model, which reinforces the idea of comparing them through the dimensionless parameter proposed in Equation (10).

Table 5. Critical damage for uncoupled damage models.

Damage Model	Critical Damage
Freudenthal	269.0 MPa
Cockcroft and Latham	324.0 MPa
Rice and Tracey	0.373

Parameters of the bilinear damage model are obtained from cyclic loading–unloading tests. Figure 5a shows the elongation over time results obtained using digital image correlation and Figure 5b presents the force over time results measured by the load cell. Both independent signals are synchronized using a python script, and from these results, the stress–strain curve is constructed, which allows for the calculation of damage through the degradation of the elastic modulus during each unloading. The characteristic parameters of the bilinear damage model are presented in Table 6. The determination of these parameters for the wire rods was previously presented by González et al. [25] following the procedure described previously in Section 2.

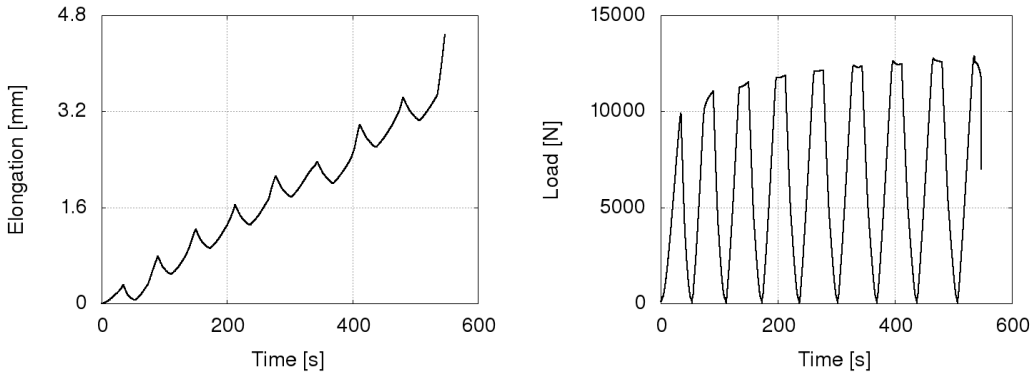

(**a**) (**b**)

Figure 5. Load–unload tensile test: (**a**) elongation vs. time and (**b**) load vs. time.

Table 6. Bilinear coupled damage parameters of 2011 aluminum alloy.

$\bar{e}_0$	$\bar{e}_i$	d_i	$\bar{e}_c$	d_c	β_d
0.02	0.065	0.120	0.257	0.154	1.500

3.2. Wire Drawing

3.2.1. Wire Drawing Forces

As mentioned previously, each drawing case was tested three times. In Figure 6, an example of the experimental forces obtained in the wire drawing process is presented. As observed, the experimental force values are not strictly constant, so Table 7 presents the average experimental drawing force for each of the 20 cases studied and also the error gap to quantify the data dispersion in this zone. As the process progresses, the force value fluctuates due to various factors, the most significant being a non-uniform distribution of lubricant on the contact surface [6] which causes oscillations in the measured force. This is more noticeable for smaller angles with high reductions where a larger contact surface is generated. Note that these types of variations are not periodic. According to the literature, when force oscillations are periodic, it could indicate that central bursting is occurring within the wire rod [12].

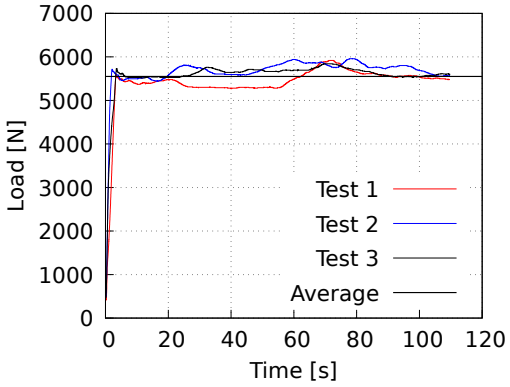

Figure 6. Example of evolution of drawing forces for the three repetitions conducted in the case of a15r38.

Table 7. Experimental drawing forces.

Reduction (%)	Angle (°)	Exp. Forces (N)
21	10	3282.5 ± 279.8
	15	3528.6 ± 264.6
	21	3868.1 ± 166.6
	27	4111.7 ± 181.3
	34	4238.0 ± 166.6
29	10	4800.3 ± 779.1
	15	4255.6 ± 387.1
	21	4571.9 ± 514.5
	27	4745.5 ± 744.8
	34	5148.8 ± 504.7
31	10	4738.4 ± 558.6
	15	4678.3 ± 725.2
	21	4874.6 ± 210.7
	27	5064.5 ± 205.8
	34	5290.7 ± 186.2
38	10	5954.7 ± 750.2
	15	5550.1 ± 347.4
	21	5664.3 ± 416.5 *
	27	5584.2 ± 215.6 **
	34	N.R. ***

* Two out of three tests were recorded. The third one reached fracture. ** One out of three tests was recorded. The other two reached fracture. *** All three cases reached fracture. The force could not be recorded.

3.2.2. Experimental DLD

A classic drawing limit diagram is presented in Figure 7. Cases that did not fracture are indicated with blue circles and cases that did fracture are marked with red crosses. The numbers positioned above the red crosses represent the quantities of fractures observed in each case. Specifically, in the case of a21r38, a fracture was observed in one out of the three tested wire rods. For the case of a27r38, fractures were observed in two out of the three tested wire rods. In the case of a34r38, fractures were observed in all three tested wire rods; thus, the force could not be recorded (N.R.). An example of each fractured case is presented in Figure 8.

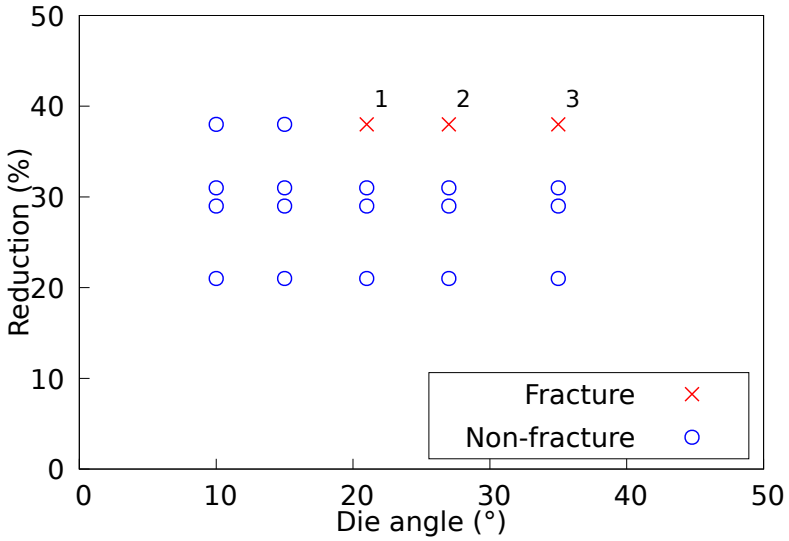

Figure 7. Experimental drawing limit diagram for Al2011 wire rods. The numbers indicated in the figure represent the number of fractures obtained.

(**a**) (**b**) (**c**)

Figure 8. Fracture in drawn wires: (**a**) case a21r38, (**b**) case a27r38, and (**c**) case a34r38.

3.2.3. Numerical 3D-DLD

The evaluation of damage according to different models (coupled and uncoupled) is subsequently presented to assess their capability to predict fracture in the drawing process. Emphasis is placed on a novel approach for presenting results where the level of damage reached for each angle and reduction in drawing is indicated using three-dimensional graphs. As far as we know, the traditional method of presenting these results involves a two-dimensional plot (angle versus reduction) where fracture and non-fracture cases are shown using appropriate symbols. In this new approach, the damage index is evaluated, which not only provides a prediction of fracture but also offers greater sensitivity to the value reached in each case.

The results obtained from each of the numerical wire drawing simulations are presented below in Figure 9 and summarized in Table 8. The damage index for each uncoupled damage model is shown in three-dimensional graphs to simultaneously evaluate the response of the model to variations in die angles and reductions. This method of presenting the results allows for a visual estimation of the value reached in each geometric configuration and its proximity to the critical condition.

The results are presented in the following figures according to the Freudenthal model (Figure 9a), the Cockcroft and Latham model (Figure 9b), the Rice and Tracey model (Figure 9c), and the bilinear coupled model (Figure 9d).

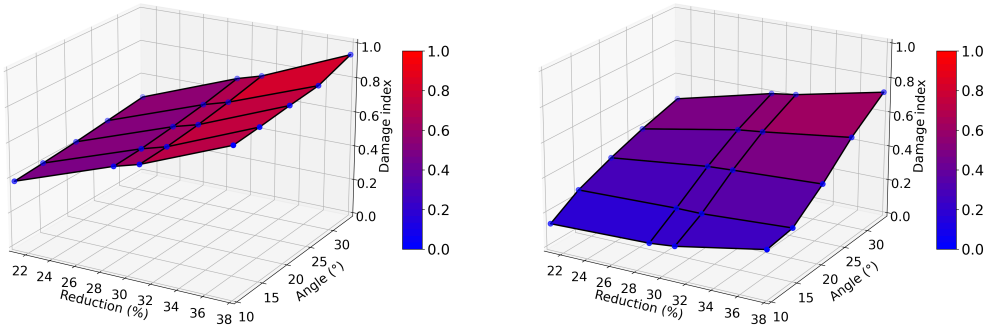

(**a**) Freudenthal (**b**) Cockcroft and Latham

Figure 9. *Cont.*

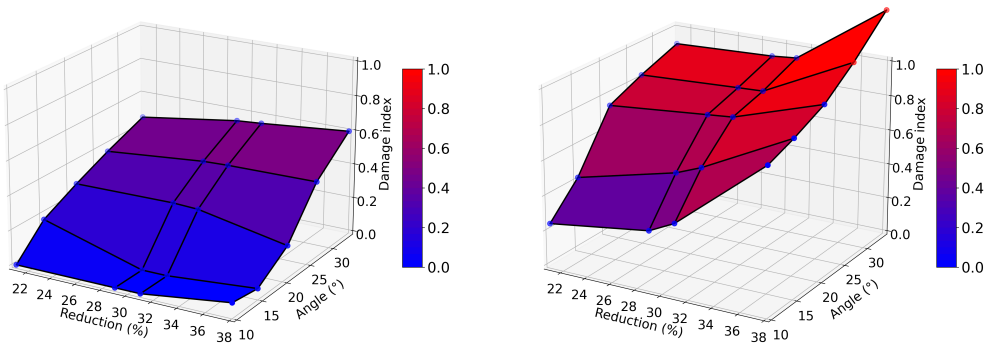

(**c**) Rice and Tracey (**d**) Bilinear coupled model

Figure 9. 3D-DLD according to different damage models for predicting fracture in the wire drawing process.

Table 8. Damage index according to different damage models for predicting fracture in the wire drawing process.

Reduction (%)	Angle (°)	Freud.	C. and L.	R. and T.	Bilinear
21	10	0.380	0.135	0.000	0.240
	15	0.394	0.237	0.169	0.415
	21	0.413	0.318	0.270	0.733
	27	0.437	0.387	0.360	0.818
	34	0.465	0.454	0.452	0.900
29	10	0.583	0.152	0.000	0.324
	15	0.592	0.254	0.000	0.558
	21	0.614	0.384	0.276	0.785
	27	0.641	0.493	0.413	0.844
	34	0.682	0.592	0.537	0.922
31	10	0.623	0.167	0.000	0.396
	15	0.632	0.254	0.000	0.616
	21	0.653	0.392	0.269	0.798
	27	0.682	0.509	0.418	0.850
	34	0.723	0.612	0.548	0.935
38	10	0.828	0.264	0.069	0.818
	15	0.839	0.284	0.044	0.876
	21	0.856	0.417	0.168	0.961
	27	0.869	0.575	0.423	1.100
	34	0.936	0.719	0.596	1.292

4. Discussion and Analysis of Results

As observed in Figure 9a, the Freudenthal model shows a consistent increase in the damage index with the increase in both angles and reductions, providing the best description of the process among all the uncoupled models. However, while it captures the general trend, it falls short of fully describing the complexity of the damage process. The Cockcroft and Latham model (Figure 9b) also highlights an increase in the damage index with both increasing angles and reductions. Nevertheless, the predicted values are lower than expected based on the experimental data, indicating a discrepancy between the model and observed results. In contrast, the Rice and Tracey model (Figure 9c) shows a clear growth trend in the damage index with increasing angles; however, it does not exhibit significant changes in response to variations in reductions, limiting its ability to accurately represent the process under different conditions.

The bilinear coupled model (Figure 9d) reproduces the experimental data accurately, particularly for the highest reduction. For the larger die angles (a27r38 and a34r38),

the model predicts that the critical damage condition is exceeded, while, for a21r38, the damage index is close to the critical value. This result aligns with experimental evidence where only one of the three tested rods is fractured in this configuration. One key feature of the bilinear coupled model is that, once the critical damage condition is reached, the damage evolves rapidly. This explains the high damage indices observed in the cases with the larger angles and higher reductions. Furthermore, the model effectively captures the variations in damage response due to changes in both die angles and reductions, demonstrating its accuracy in predicting critical damage conditions.

The Freudenthal, Cockcroft and Latham, and Rice and Tracey models are well known and widely used in metal damage prediction. However, the proposed bilinear coupled model, an extension of Lemaitre's classic model, offers several advantages, particularly in capturing damage evolution under varying loading conditions. While traditional models rely on a single phase of damage accumulation, the bilinear coupled model accounts for two distinct phases, each modeled through linear functions, providing a more accurate representation of the behavior of the material during complex processes like wire drawing. The bilinear formulation is coupled, meaning that the accumulated damage directly influences the mechanical response of the material, resulting in a more realistic simulation of the degradation of properties due to plasticity. Despite these advantages, the main limitation of the bilinear coupled model is its higher computational cost compared to uncoupled models, as the damage at each time step affects the constitutive equations, increasing computational complexity. Moreover, the experimental characterization of this model requires more expensive cyclic load–unload tensile tests (though still manageable) unlike the simpler monotonic uniaxial tests used for uncoupled models. Additionally, a detailed characterization is needed to accurately model the period between the initiation of fracture and the final separation of the specimen. This zone is represented by a potential function that produces a sharp increase in damage with minimal strain increments, and its precise characterization remains a challenge due to occurring over a short time frame.

5. Conclusions

In this study, a comprehensive damage analysis was applied to the wire drawing process of 2011 aluminum alloy wire rods through both experimental and numerical approaches. Two damage modeling approaches were utilized: uncoupled damage models and a bilinear coupled damage model. The numerical results obtained with the bilinear coupled model demonstrated a good correlation with the reported experimental results. In contrast, the results obtained with the uncoupled damage models did not accurately reproduce the experimental trends. These models tended to underestimate the damage values, failing to reflect the observed increase in damage with higher reductions and angles. The bilinear coupled damage model proved to be more effective in predicting damage in the wire drawing process of 2011 aluminum alloy wire rods. The ability of this model to closely match experimental observations and accurately reflect the effects of both angles and reductions on damage makes it a valuable tool for improving industrial practices and material performance evaluations.

Additionally, a novel three-dimensional visualization scheme was presented to illustrate the relationship between damage and the geometric variables of the wire drawing process. This approach provides a better approximation of the results, allowing for a more intuitive and comprehensive understanding of how angles and reductions influence the damage index.

Author Contributions: Conceptualization, Á.G., D.C. and M.C.; methodology, Á.G., D.C. and M.C.; software, Á.G. and D.C.; validation, Á.G., D.C., M.C. and J.-P.P.; formal analysis, Á.G., D.C., M.C. and J.-P.P.; investigation, Á.G.; resources, D.C.; data curation, Á.G.; writing—original draft preparation, Á.G.; writing—review and editing, Á.G., D.C., M.C. and J.-P.P.; visualization, Á.G.; supervision, D.C. and M.C.; project administration, D.C.; funding acquisition, D.C. All authors have read and agreed to the published version of the manuscript.

Funding: This research was financially supported by the Chilean Agency of Research and Development (ANID) through the Fondecyt Project 1220211 and the Wallonie Bruxelles International collaboration project No. 5.

Institutional Review Board Statement: Not applicable.

Data Availability Statement: The data will be available under request to the authors.

Acknowledgments: The support provided by the National Agency of Research and Development ANID through FONDECYT Project No. 1220211 and the Wallonie Bruxelles International collaboration project 5 are gratefully acknowledged.

Conflicts of Interest: The authors declare no conflicts of interest.

References

1. Badi, R.; Bensaada, S.; Tala-Ighil, N.; Lebaal, N. Numerical analysis of the effects of incremental reduction rate in the wire drawing process. *Int. J. Adv. Manuf. Technol.* **2024**, *133*, 5197–5209. [CrossRef]
2. Ma, A.; Zhang, Y.; Dong, L.; Yan, H.; Fang, F.; Li, Z. Damage and fracture analyses of wire with off-center inclusion on multi-pass drawing under different back tensions. *Eng. Fail. Anal.* **2022**, *139*, 106512. [CrossRef]
3. Ma, A.; Cheng, J.; Wei, D.; Li, Q.; Fang, F.; Li, Z. Experiments and numerical analyses on splitting fracture of wire under multi-pass drawing. *Eng. Fail. Anal.* **2022**, *134*, 106035. [CrossRef]
4. Kubík, P.; Petruska, J.; Judas, J.; Šebek, F. Computational prediction of chevron cracking during multi-pass cold forward extrusion. *J. Manuf. Process.* **2023**, *102*, 154–168. [CrossRef]
5. Alexandrov, S.; Hwang, Y.-M.; Tsui, H.S.R. Determining the Drawing Force in a Wire Drawing Process Considering an Arbitrary Hardening Law. *Processes* **2022**, *10*, 1336. [CrossRef]
6. Radionova, L.V.; Gromov, D.V.; Lisovskiy, R.A.; Erdakov, I.N. Experimental Determination and Calculation of the Wire Drawing Force in Monolithic Dies on Straight-Line Drawing Machines. *Machines* **2023**, *11*, 252. [CrossRef]
7. Hwang, J.-K. Comparison of Temperature Distribution between TWIP and Plain Carbon Steels during Wire Drawing. *Materials* **2022**, *15*, 8696. [CrossRef]
8. Wu, H.; Huang, T.; Song, K.; Li, S.; Zhou, Y.; Zhang, Y. Effect of drawing speed on the deformation characteristics, microstructure and properties of copper wire rod. *Mater. Sci. Eng. A* **2024**, *892*, 146025. [CrossRef]
9. Alberti, N.; Barcellona, A.; Masnata, A.; Micari, F. Central Bursting Defects in Drawing and Extrusion: Numerical and Ultrasonic Evaluation. *Ann. CIRP* **1993**, *42*, 269–272. [CrossRef]
10. Oyane, M.; Sato, T.; Okimoto, K.; Shima, S. Criteria for Ductile Fracture and Their Applications. *J. Mech. Work. Technol.* **1980**, *4*, 65–81. [CrossRef]
11. Reddy, N.V.; Dixit, P.M.; Lal, G.K. Ductile Fracture Criteria and Its Prediction in Axisymmetric Drawing. *Int. J. Mach. Tools Manuf.* **2000**, *40*, 95–111. [CrossRef]
12. McAllen, P.; Phelan, P. Ductile Fracture by Central Bursts in Drawn 2011 Aluminium Wire. *Int. J. Fract.* **2005**, *135*, 19–33. [CrossRef]
13. Orbegozo, J.I. Fracture in Wire Drawing. *Ann. CIRP* **1968**, *16*, 319–330.
14. Haddi, A.; Imad, A.; Vega, G. The influence of the drawing parameters and temperature rise on the prediction of chevron crack formation in wire drawing. *Int. J. Fract.* **2012**, *176*, 171–180. [CrossRef]
15. Cockcroft, M.; Latham, D. Ductility and workability of metals. *J. Inst. Met.* **1968**, *96*, 33–39.
16. Cho, D.; Jang, Y.-C.; Lee, Y. Evaluation of the prediction ability of ductile fracture criteria over a wide range of drawing conditions. *J. Mech. Sci. Technol.* **2019**, *33*, 4245–4254. [CrossRef]
17. Cho, D.; Lee, Y. Development of a machine learning based fast running model to determine rapidly the process conditions in drawing process. *Int. J. Automot. Technol.* **2019**, *20*, 9–17. [CrossRef]
18. Ko, Y.K.; Lee, J.S.; Huh, H.; Kim, H.K.; Park, S.H. Prediction of fracture in hub-hole expanding process using a new ductile fracture criterion. *J. Mater. Process. Technol.* **2007**, *187–188*, 358–362. [CrossRef]
19. Roh, Y.-H.; Cho, D.; Choi, H.-C.; Yang, Z.; Lee, Y. Process Condition Diagram Predicting Onset of Microdefects and Fracture in Cold Bar Drawing. *Metals* **2021**, *11*, 479. [CrossRef]
20. Kachanov, L. Rupture time under creep conditions. *Int. J. Fract.* **1999**, *97*, 11–18. [CrossRef]
21. Freudenthal, A. *The Inelastic Behaviour of Engineering Materials and Structures*; John Wiley & Sons: Hoboken, NJ, USA, 1950.
22. Rice, J.R.; Tracey, D.M. On the Ductile Enlargement of Voids in Triaxial Stress Fields. *J. Mech. Phys. Solids* **1969**, *17*, 201–217. [CrossRef]
23. Lemaitre, J. A Continuous Damage Mechanics Model for Ductile Fracture. *J. Eng. Mater. Technol.* **1985**, *107*, 83–89. [CrossRef]
24. Celentano, D.J.; Chaboche, J.-L. Experimental and numerical characterization of damage evolution in steels. *Int. J. Plast.* **2007**, *23*, 1739–1762. [CrossRef]

25. González, Á.A.; Cruchaga, M.A.; Celentano, D.J. Bilinear damage evolution in AA2011 wire drawing processes. *Int. J. Damage Mech.* **2022**, *31*, 645–664. [CrossRef]
26. González, Á.; Celentano, D.; Cruchaga, M.; Ponthot, J.-P. The Triaxiality Effect on Damage Evolution in Al-2024 Tensile Samples. *Metals* **2024**, *14*, 1103. [CrossRef]